Fault Tolerant Control of Advanced Power Generation Center for More-Electric Aircraft Applications *(In Windows/Microsoft Word)*

Xiaoyu Lang, Tao Yang, *Senior Member, IEEE,* Zhenyu Wang, Cheng Wang, Serhiy Bozhko, *Senior Member, IEEE,* and Patrick Wheeler, *Fellow, IEEE*

Abstract: This paper presents a control scheme for a recently reported aircraft advanced power generation center (APGC) during postfault operation conditions. Within the APGC, two electrical generators extract power from two separate engine shafts and supply electrical power to a common HVDC bus through their dedicated main AC/DC power converters. An extra back-to-back (BTB) converter is also used to connect the ac terminals of the two generators. This architecture provides merits of fault tolerance capabilities of the APGC. In the case of main AC/DC power converter failure, the system can be reconfigured and the BTB converter provides an extra power flow path from the generators to the HVDC bus. This ensures electrical power generation capabilities onboard. The paper discusses in detail the control of the APGC under fault conditions with one main AC/DC converter failure. A seamless transition scheme from normal operation to postfault conditions is proposed using a voltage command initialization technique within the BTB converter. Both experimental and simulation results have verified the fault tolerance improvement and control performances of the APGC.

Index Terms: Fault tolerance, power control, more-electric aircraft, seamless transition, back-to-back converter.

I. Introduction

The more-electric aircraft (MEA) concept is a major trend in the modern aerospace industry due to the advantages of high efficiency, low maintenance cost, and benefits to the environment. Much conventional onboard equipment consuming pneumatic, mechanical, and hydraulic energies will be replaced by their electrical counterparts. As a result the electric power demand increases significantly and this introduces challenges in designing a suitable electrical power generation center (PGC) [1].

Conventionally, an electrical generator is coupled with the engine high-pressure spool (HPS) due to its relatively constant speed [2]. However, with the increase of electrical loads onboard, this single-generator structure has difficulty in meeting the increased electrical power demand of the MEA. Furthermore, electrical power extracted from the engine HPS is also limited as excessive power extraction will undermine the efficiency and stability of the engine [3].

An effective way to address these challenges is to use another generator on the low-pressure spool (LPS) of the engine. With both spools supplying electrical power to the downstream loads, more power becomes available. Furthermore, adding an extra generator will improve the redundancy of the power generation system. To fully explore the advantages of this dual-generator system, a common dc-
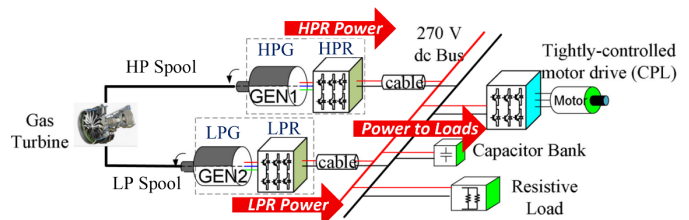
Fig. 1. Electrical power generation center (PGC) with two generators and a single dc bus.

bus architecture has been proposed in recent studies [4]-[7] as shown in **Fig. 1**. Compared with ac systems, the dc system emerges as a superior option in terms of efficiency and weight. The dc network also allows parallel operation of multiple sources, such as the generator on the low-pressure spool (LPG), the generator on the high-pressure spool (HPG), and the auxiliary power unit [8]. Moreover, energy storage devices can be integrated, realizing peak shaving of the power demand [9].

Although the power generation center in **Fig. 1** shows advantages in terms of controllability and efficiency, there are two critical constraints. One is the field-weakening (FW) operation of the HPG. Since the HPS is running at a high speed (close to 20,000rpm in the high-speed settings of engine [10]), the coupled HPG will induce a high back electromotive force (back EMF), which requires the associated HPR to provide a high ac voltage to handle the back EMF. However, due to the limited dc-link voltage (270V as per [11], [12]), the ac voltage of the HPR is also limited, which causes difficulties in handling the high back EMF of the HPG. To address this problem, FW operation is developed for the HPG in high-speed conditions to limit the stator voltage considering the limited dc-link voltage [13]. FW current needs to be injected into the permanent magnet machine based HPG to reduce the rotor flux beyond the base speed. However, the negative effect is that the FW current will circulate in the path of the HPG and the HPR, resulting in considerable copper loss in the HPG, and increasing conduction and switching losses in the HPR.

Another critical constraint of the architecture in **Fig. 1** is the poor fault tolerance capability in terms of power conversion. In traction and power generation related systems, power converters are identified as the most vulnerable parts in terms of reliabilities [14], [15]. If contingency such as open-circuit fault occurs to the low-pressure channel or high-pressure channel rectifiers (LP rectifier, i.e., LPR, and HP rectifier, i.e., HPR) in **Fig. 1** due to gate-driver fault or cycling high currents, the faulty rectifier needs to be stopped and disconnected from the dc grid [16]. However, the associated generators cannot be shut down suddenly as they are connected to the aircraft engine, which has a significant inertia. Moreover, even if the generators are stopped smoothly, these generators are no longer available for the

electrical loads. This will undermine the power generation capability and thus limit large-scale applications of onboard electrical equipment. Furthermore, losing one generator may lead to severe system instability at high load power scenarios [4].

To enhance the reliability of a permanent-magnet synchronous generator (PMSG) based power generation system, much research has been focused on the fault tolerance control for the main rectifiers. For example, in the case of a single-phase open-circuit fault of a three-level rectifier, fault tolerance is achieved using redundant voltage vectors to synthesize the targeted voltage vector [17], [18]. In [19], a carrier-based pulse-width modulation with zero-sequence voltage injection is proposed to reduce current distortion in the case of open-circuit failure. Although these methods do not require additional hardware setup, the rectification performance in the healthy state cannot be fully restored. In order to achieve the same control performance as in a healthy state, a redundant phase leg is deployed to replace the faulty phase leg hence a healthy three-phase rectifier can be reconstructed [20], [21]. However, this method requires additional power modules and switches.

Although the above-mentioned strategies can provide fault tolerance control, they are only effective in addressing the single-phase fault. In practice, due to the power modules of the three-phase legs being spatially close, when one leg fails due to high ambient temperature or high current, other legs are also prone to failure. The above-mentioned fault tolerance methods are not suitable to deal with this multi-phase failure situation, but an effective solution is to deploy multiple redundant phase legs or multiple converters in parallel. However, this will undoubtably increase the overall cost [22], [23].

To deal with the constraint of high FW current and the requirement of fault tolerance, an advanced power generation center (APGC) was proposed in our previous work [24], [25], as shown in **Fig. 2**. A back-to-back (BTB) converter connects the original dual power generation channels shown in **Fig. 1**. With this configuration, the following benefits can be achieved:

(1) The HPG can operate at high speeds without FW. This is achieved due to a high internal dc-link voltage in the BTB converter. With no FW current injected into the HPG, it significantly reduces power loss of the HPG and the HPR.

(2) An improved fault tolerance capability and system availability. In the case of either HPR or LPR failure, the BTB converter can provide an additional power flow path for the generators, allowing the two generators to continue operating and supplying power and services to the downstream loads.

The characteristics of FW elimination have been investigated in [24], [25], where a 5% efficiency improvement is achieved. As a continuation of our earlier work, this paper will focus on the realization of the fault tolerance enhancement and the associated fault tolerant control. It should be noted that despite the incorporation of an extra BTB converter in the APGC, the two objectives of FW elimination and improved fault tolerance are achieved at the same time. Therefore, deploying a BTB converter is considered better than the solutions which add parallel converters [22], [23].

Since there are multiple power converters, generators, and various loads in the system of **Fig. 2**, proper control design in both healthy and postfault operation state is of great importance. The rest of this paper is organized as follows. Control schemes for the overall system are developed in Section II to make those power converters coordinated in the healthy state. Section III illustrates the system reconfiguration at either HPR or LPR failures. A voltage command initialization strategy is applied to the BTB converter to avoid the abrupt change in the generators' currents when transiting from the healthy state to postfault operation state. Experimental and simulation results are presented and discussed in Section IV. Section V presents considerations of the APGC in the practical application. Section VI concludes this paper.

II. System Description and Basics of Control Design Under Normal Operation Conditions of the APGC

As can be seen in **Fig. 2** an extra back-to-back (BTB) converter is used, providing an extra power flow path between the HP generator and the LP generator compared with the power generation center in **Fig. 1**. This configuration allows power transfer between the HP channel and LP channel. More importantly, the BTB converter provides a power flow path to the main HVDC bus for the remaining generator in the case of rectifier failure. Hence generators can supply continuous power to the onboard loads and the fault tolerance of the overall system is improved.

A description of the circuitry configuration is elaborated in this section. Moreover, although control schemes for the APGC under normal conditions have been discussed in our previous publication [24], some of the key findings (especially control of the four AC/DC converters) will be briefly introduced in this session to make this paper self-contained.

A. Circuitry Configuration Analysis

It can be seen from **Fig. 2** that the four power converters, i.e., HPR, LPR, BTB_1 converter and BTB_2 converter, are all voltage source converters (VSC). To enable them to operate compatibly, inductors should be deployed to separate these VSCs. Moreover, inductors can filter high frequency pulse-width modulation harmonics generated by the switching actions of power devices. There are four possible configurations in total with different locations of inductors, as shown in **Fig. 3**.

In **Fig. 3**(a) and (b), an inductor, denoting as L_2, is placed at the front end of the BTB_2 converter close to the HPG side. In these cases, the terminal voltages of the HPG are limited within $\frac{v_{dc}}{\sqrt{3}}$ using the typical space vector pulse-width modulation (SVPWM) [10], where v_{dc} is the main HVDC bus voltage. The value of v_{dc} is considered as 270V to follow the MIF-STD-704F standard. Hence, for some permanent magnet-based generators, such as the AEGART electrical machine developed under the frame of the Clean Sky project [26], it means that FW operation is still needed for the HPG with the configurations shown in **Fig. 3**(a) and (b).

In **Fig. 3**(c) and (d), L_2 is deployed at the front of the HPR. In this case, terminals voltages of the HPG are limited within $\frac{v_{BTB}}{\sqrt{3}}$ using the SVPWM, where v_{BTB} is the dc-link voltage within the BTB converter. By increasing the voltage
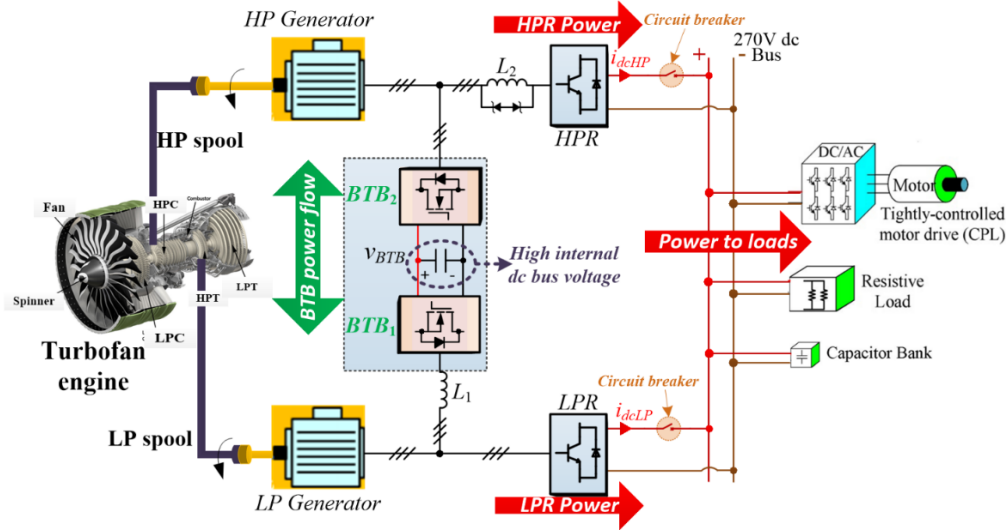
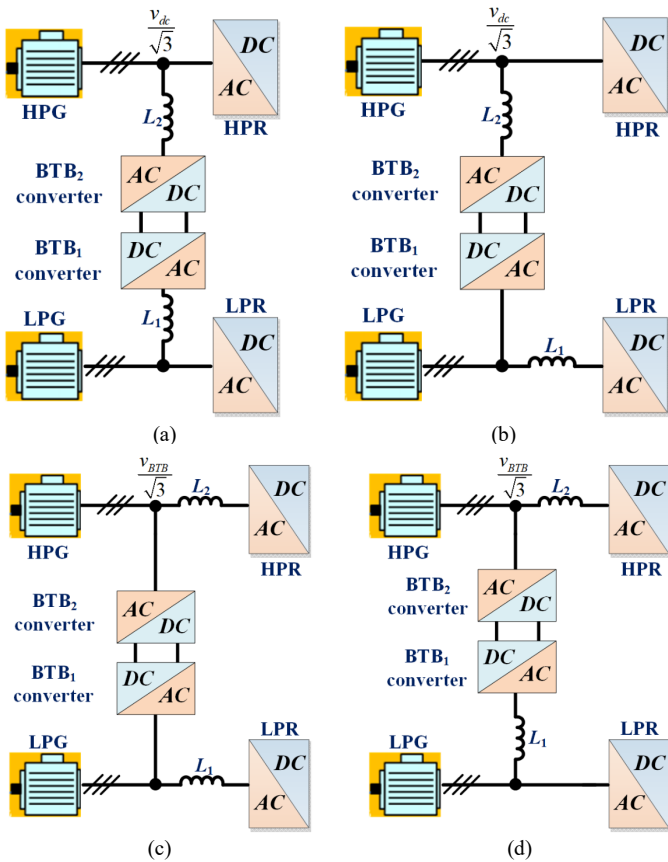Fig. 2. The architecture of the APGC with a back-to-back converter [24], [25].

(a)   (b)

(c)   (d)

Fig. 3. The four configurations with different locations of inductors.

B. Control Design for The Rectifiers in a Normal Operation Condition

Under normal operation conditions, the two main rectifiers (HPR and LPR) connected to the main HVDC grid shared the same control scheme presented in **Fig. 4**. It can be seen that a classical cascaded control structure has been implemented with the inner loop controlling the d-axis and q-axis currents. The outer loop is to control the dc currents injected by the HPR and LPR to the HVDC bus. A droop control is adopted to manage the power sharing between the HPR and the LPR because it does not need communication links [4], [27]. In **Fig. 4**, the dc current reference is generated according to a predefined *V-I* droop characteristic, which is shown as follows

$$i_{dcLP}{}^{ref} = \frac{v_{dc}{}^* - v_{dc}}{g_{LP}} \qquad i_{dcHP}{}^{ref} = \frac{v_{dc}{}^* - v_{dc}}{g_{HP}} \qquad (1)$$

where g_{LP} and g_{HP} are the droop gains of the LPR and HPR controller, respectively. $i_{dcLP}{}^{ref}$ and $i_{dcHP}{}^{ref}$ are the dc current commands for the LPR and HPR, respectively. $v_{dc}{}^*$ is the nominal dc voltage, which is 270V as per the aerospace standard [12].
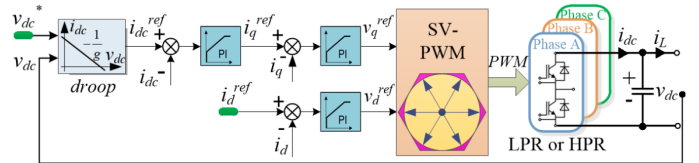

Fig. 4. Control scheme for the rectifiers.

of v_{BTB}, the HPG can operate at a high speed without field-weaking control. The difference between **Fig. 3**(c) and (d) is the location of inductor L_1. Since most power of the LP channel is delivered through the LPR to feed the dc bus loads, and a relatively small proportion of power is transferred through the BTB converter, the phase current of the LPR is larger than that of the BTB$_1$ converter. Placing L_1 at the front end of the BTB$_1$ converter instead of the LPR can reduce the power losses in the inductor L_1. To conclude the above, the configuration of inductors shown in **Fig. 3**(d) are chosen to build the APGC in **Fig. 2**.

C. Control Design for The BTB₁ Converter in The Normal Operation Conditions

In normal operation conditions, the BTB converter can be used to exchange power between the LP channel and the HP channel. As discussed in [28], power transfer from the LP shaft to the HP shaft will be inevitable if more power needs to be extracted from the engine core to supply the increasing electrical power loads for the future aircraft. The BTB converter essentially consists of two separate AC/DC converters, denoting as BTB$_1$ and BTB$_2$ converter, respectively. In this section, the control designs for the two converters are illustrated briefly.

The diagram of the LPG and LPR subsystem is presented in **Fig. 5**. Since the ac terminals of the LPG and BTB$_1$ converter share the same junctions a, b, and c, an effective way to control the transferred power from the LP channel to the BTB converter is to control the currents of LPG (i_{xLP}) and BTB$_1$ converter (i_{xBTB1}, $x=a,b,c$) to be in phase. In that case, power sharing between the LPR and BTB$_1$ converter can be achieved by proportionally controlling the magnitudes of the phase currents, i.e., controlling the magnitude ratio between the phase currents i_{xLP} and i_{xBTB1}.
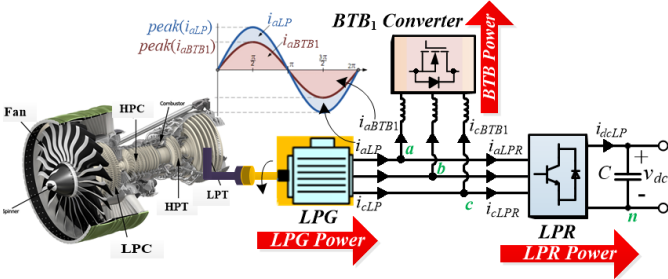

Fig. 5. The schematic of LP channel with the LPG, LPR and BTB$_1$ converter. Red arrows denote the directions of power flow.

On the other hand, the BTB$_1$ converter is also responsible for regulating the dc-link voltage v_{BTB}. To synchronize i_{xBTB1} and i_{xLP} in phase and achieve dc-link voltage v_{BTB} control, a new control structure is shown **Fig. 6**. The control scheme is able to fulfill the two functions, i.e., dc voltage regulation within the BTB converter and synchronization of the phase currents i_{xBTB1} and i_{xLP}, where $x=a,b,c$.

As can be seen in **Fig. 6**, within the BTB$_1$ converter, the d-axis and q-axis current references are dependent on the dq-axes currents of the LPG and the power ratio gain m between the LPG and BTB converter. A common d axis (LPG's rotor angle) will be used to transform the phase currents i_{xBTB1} and i_{xLP} to the i_{dBTB1}, i_{qBTB1}, i_{dLP} and i_{qLP}, respectively. By doing this, i_{xBTB1} and i_{xLP} will be synchronized in phase (see **Fig. 5**). The gain m will be the magnitude ratio of i_{xBTB1} over i_{xLP}.

If dc-link voltage v_{BTB} is smaller than its reference, the gain m, and hence i_{xBTB1} will increase, thus more power will be transferred to the BTB converter to charge the internal dc-link capacitor. On the other hand, if v_{BTB} is larger than its reference, the gain m, and hence i_{xBTB1} will decrease, thus less power will be transferred to the BTB converter and v_{BTB} will be back to the reference value. With this control strategy, v_{BTB} can be stabilized, and i_{xBTB1} and i_{xLP} can be synchronized. This control scheme is very different from the conventional active front-end control scheme [29], [30], where the output of the voltage controller is active current command or active power command. In the steady state, the power generated by the LPG, i.e., P_{LPG} and the power transferred to the BTB converter, i.e., P_{BTB} should have the following relation:

$$\frac{peak(i_{aLP})}{peak(i_{aBTB1})} = \frac{i_{qLP}}{i_{qBTB1}} = \frac{i_{dLP}}{i_{dBTB1}} = \frac{P_{LPG}}{P_{BTB}} = \frac{1}{m} \qquad (2)$$

D. Control Design for The BTB$_2$ Converter in Normal Operation Conditions

Since the HPG is coupled to the HP shaft of the engine, the rotation speed of the HPG is dependent on the HP shaft, denoting as ω_{mHP}. Then the mechanical power P_m extracted from the HP shaft can be expressed as $P_m = \omega_{mHP}T_e$, where T_e is the electromagnetic torque of the HPG. Since the speed of
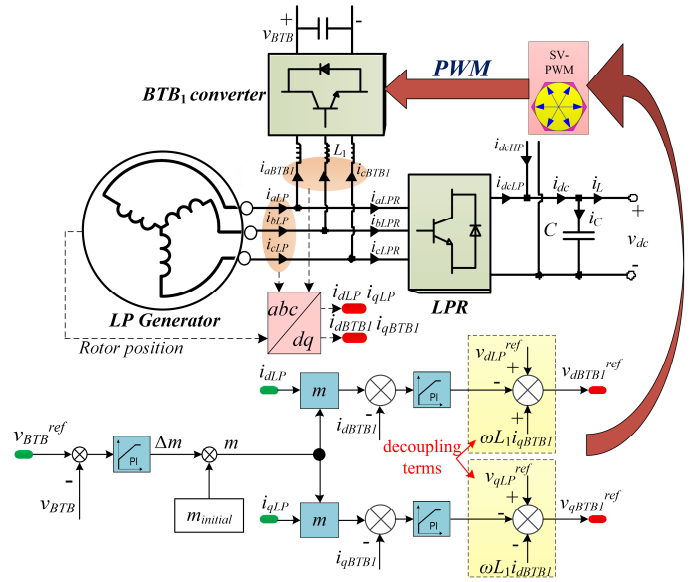

Fig. 6. The control schematic for the BTB$_1$ converter.

the HP shaft depends on the specific operation mode of the engine, to control the output power of the HPG, the only available variable that can be used is T_e.

Since the terminals of the HPG are directly connected to the BTB$_2$ converter, operation of the HPG can be controlled by the BTB$_2$ converter. For a considered surface-mounted permanent magnet machine, T_e can be expressed as [31]

$$T_e = 1.5 p \psi_f i_{qHP} \qquad (3)$$

where p is the pole pairs. ψ_f is the flux linkage of magnet. i_{qHP} is the q-axis currents of HPG.

Based on (3), the reference of i_{qHP} can be obtained as:

$$i_{qHP}{}^{ref} = \frac{P_{HPG}}{1.5 p \psi_f \omega_{mHP}} \qquad (4)$$

where P_{HPG} is the expected active power of the HPG. p and ψ_f are the machines parameters and ω_{mHP} is the mechanical angular speed of the machine which can be measured with a position sensor or estimated using a sensorless scheme. The active power of the HPG P_{HPG} is defined by the total load power requirement and the power sharing ratio between the HPG and LPG. Using this information, the i_q reference of the HPG, $i_{qHP}{}^{ref}$, can be obtained.

The HPG normally runs at a high speed (over 20 krpm). Using the system architecture in **Fig. 1**, a FW control may be needed as the machine back EMF will be high and the HVDC bus voltage is limited to 270V. Application of the BTB converter will avoid such an issue. Since the dc-link within the BTB converter is not directly connected with the onboard loads, its dc voltage can be set higher than the HVDC bus. In that case, the HPG can be operated with no need of FW. The i_d reference $i_{dHP}{}^{ref}$ can be set as 0 to realize the maximum torque per ampere control. This, in return will reduce copper loss in the HPG and thus increase the system efficiency. The control scheme for the BTB$_2$ converter is shown in **Fig. 7**.

To conclude Section II, the overall configuration and control schemes for each individual power converters in the healthy state are summarized in **Fig. 8**. The relationships of the power flow are summarized in **Table I**. To be specific, power sharing between the LPR and HPR is realized by droop control. Using droop gains g_{LP} and g_{HP}, the power
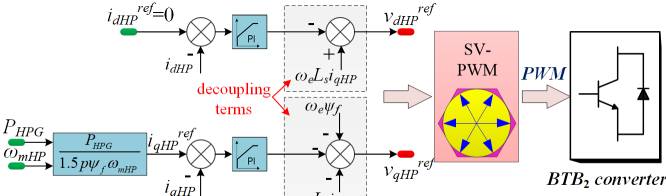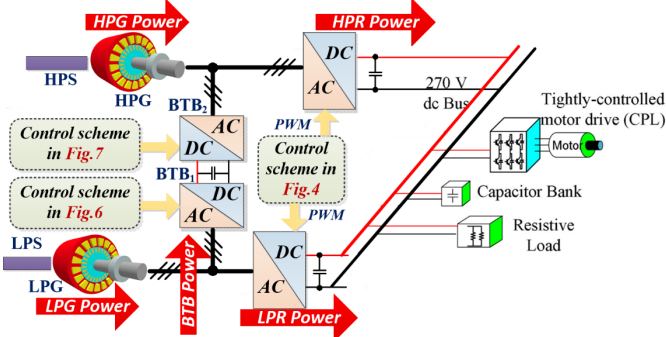
Fig. 7. Control scheme for the BTB$_2$ converter.

Fig. 8. Overall control diagram of the APGC in the healthy state.

sharing ratio can be controlled. Assuming that the ratio between the HPG's power and the total power is γ_{HP}, the output active power of the HPG (P_{HPG}) depends on the total load power and γ_{HP}. Hence, power transferred through the BTB converter compensates for the difference between the HPR's power and the HPG's power.

Table I. Relationships of power flow.

Parameter	Value	Parameter	Value
Total load power	P_t	HPG's Power	$P_t \times$ HPG's power sharing ratio = $\gamma_{HP} \cdot P_t$
HPR's Power	$\dfrac{g_{LP} \cdot P_t}{g_{HP} + g_{LP}}$	LPG's Power	Total power – HPG's Power = $(1 - \gamma_{HP}) P_t$
LPR's Power	$\dfrac{g_{HP} \cdot P_t}{g_{HP} + g_{LP}}$	BTB's Power	HPR's Power – HPG's Power = $\dfrac{g_{LP} \cdot P_t}{g_{HP} + g_{LP}} - \gamma_{HP} P_t$

III. System Reconfiguration and Control Schemes with Seamless Transition at Rectifier Failures

As mentioned previously, one of the key advantages of the APGC is its fault tolerant capabilities. The BTB converter provides flexibility to reconfigure the APGC after rectifier failures. During the transition from normal operation state to fault and then postfault operation states, the torque of generators may change abruptly. This needs to be avoided as the abrupt change of generator torque may have significantly negative impact on aircraft engines. To cope with this issue,

system reconfiguration with seamless transition from normal to postfault operation conditions is essential and will be developed in this section.

A. System Reconfiguration and Seamless Transition Scheme at LP Rectifier Failure

Once a fault within the LPR is detected, the circuit breaker at the LPR's dc side can disconnect the LPR from the HVDC grid. The rest of the system will be reconfigured as shown in **Fig. 9**. In the postfault operation conditions, all of the power of the LPG is transferred to the HP channel and then fed to the main dc bus by the HPR. The LPG will continuously supply power to the HVDC grid. The impacts of failure to the electrical loads will need to be minimized with smooth reconfiguration transition.

After reconfiguration, the HPR control will be amended to stabilize the main dc bus voltage. As can be seen in **Fig. 9**, the inner loop of the HPR control is i_{dHPR} and i_{qHPR} control, where i_{dHPR} and i_{qHPR} are the currents (in the dq frame) flowing into the HPR. The outer loop is to maintain the main dc bus at the reference level (270V in this case). The droop control used for power sharing for the HPR is deactivated as the paralleled LPR is no longer available.

The BTB$_1$ converter control will also need to be changed and will be running as an active front-end to regulate the internal dc-link voltage v_{BTB} within the BTB converter. No managed power transfer is required any more as all the power from the LPG will be routed through the BTB converter. The inner loop of the BTB$_1$ converter is i_{dLP} and i_{qLP} control, where i_{dLP} and i_{qLP} are the dq currents of the LPG. The outer loop is the dc-link voltage v_{BTB} control. For the BTB$_2$ converter, the control scheme presented in Section II-C remains to regulate the active power of the HPG. To summarize, the BTB$_1$ converter is used for stabilizing the dc voltage within the BTB converter, and the control for the BTB$_2$ converter is to regulate the HPG's power.

From the viewpoint of power, there are two essential electrical power sources in the reconfigured system, i.e., the HPG and LPG. The HPG's power can be actively managed by controlling its torque as its speed is dependent on the aircraft engines. The LPG's power is transferred from the LP to HP channel through the BTB converter. The LPG automatically compensates for the difference between the total load power and the HPG's power. The functions and control objectives of each converter before and after fault are summarized in **Table II**.
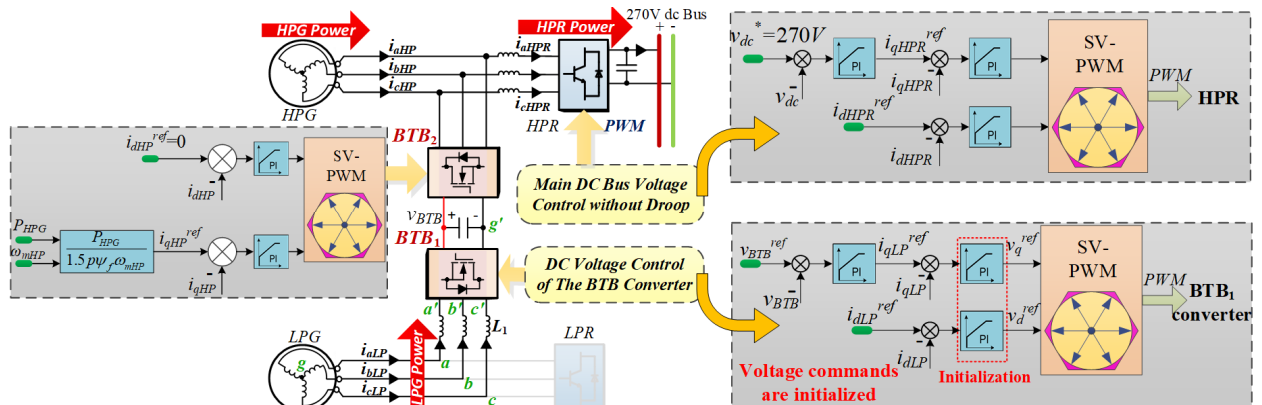

Fig. 9. The power flow diagram and control schemes at LP rectifier fault.

Table II. Functions and control objectives for each remaining converter when the LPR is disconnected due to fault.

Remaining power converter	Functions	Control objectives	
		Before fault	After fault
HPR	Delivering power to the main dc bus, feeding onboard loads.	Sharing load power under droop control (see **Fig. 4**)	Stabilizing the main dc bus voltage to 270V (see **Fig. 9**)
BTB$_1$ converter	Providing an additional power flow path to the LPG when LPR is disconnected.	Synchronize the phase currents and stabilize the dc voltage of the BTB converter (see **Fig. 6**)	Stabilizing the internal dc-link voltage (see **Fig. 9**)
BTB$_2$ converter	Controlling the operating state and power of the HPG.	Controlling the dq-axes currents of the HPG to generate active power P_{HPG} (see **Fig. 7**)	Controlling the dq-axes currents of the HPG to output power P_{HPG} (see **Fig. 9**)

Directly disconnecting the LPR from the HVDC grid after fault will result in an abrupt change of the LPG's terminal voltages and thus draw excessive currents from the LPG. This, in return, will lead to an undesired torque. In the worst case, it could damage the engine shaft. To avoid this and to achieve a seamless transition between normal and postfault operations, the terminal voltages of the LPG should remain unchanged during this transition. Since the LPG's ac terminals and the BTB$_1$ converter's ac terminals are connected through a filter L_1, maintaining the LPG's ac terminal voltages can be achieved by actively controlling the BTB$_1$ converter's terminal voltages.

The equivalent circuit of the LPG-BTB$_1$ converter subsystem after fault is built in **Fig. 10**. The definitions of variables and nodes are shown in **Fig. 9**, where v_{ag} is the phase-to-neutral voltage of the LPG, $v_{a'g'}$ is the leg voltage of the BTB$_1$ converter, L_1 and R_1 are the inductance and equivalent resistance of the filter whose voltage drop is $v_{aa'}$.
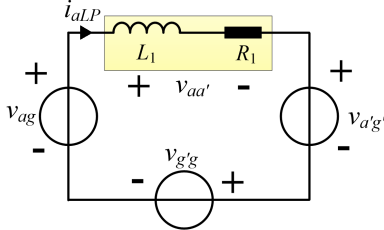
Fig. 10. The equivalent circuit of a-phase of the LPG-BTB$_1$ converter subsystem.

Based on **Fig. 9** and **Fig. 10**, the following relations can be derived:

$$\begin{cases} v_{xg} = R_1 i_{xLP} + L_1 \dfrac{di_{xLP}}{dt} + v_{x'g'} + v_{g'g}, \ x = a,b,c \ \text{(i)} \\ \sum_{x=a,b,c} i_{xLP} = \sum_{x=a,b,c} v_{xg} = 0 \hspace{1.5cm} \text{(ii)} \end{cases} \quad (5)$$

Adding the three equations in (i) and considering (ii), the voltage difference between the reference points g' at the BTB dc-link side and the LPG's neutral point g can be obtained as

$$v_{g'g} = -\frac{1}{3} \sum_{x=a,b,c} v_{x'g'} \quad (6)$$

Applying the abc/dq transformation to (5) and considering (6), the electrical relationship of the LPG-BTB$_1$ converter subsystem in the dq frame can be derived as follows:

$$\begin{cases} v_{dLP} = R_1 i_{dLP} + L_1 \dfrac{di_{dLP}}{dt} + v_{dBTB1} - \omega_{eLP} L_1 i_{qLP} \\ v_{qLP} = R_1 i_{qLP} + L_1 \dfrac{di_{qLP}}{dt} + v_{qBTB1} + \omega_{eLP} L_1 i_{dLP} \end{cases} \quad (7)$$

where v_{dLP} and v_{qLP} are the LPG's dq-axes terminal voltages. i_{dLP} and i_{qLP} are the dq currents of the LPG. v_{dBTB1} and v_{qBTB1} are the ac voltages of the BTB$_1$ converter in the dq frame. Using the first-order Taylor expansion, (7) can be discretized as follows:

$$\begin{bmatrix} v_{dBTB1}(k) \\ v_{qBTB1}(k) \end{bmatrix} = \begin{bmatrix} v_{dLP}(k) \\ v_{qLP}(k) \end{bmatrix} + \begin{bmatrix} L_1/T_s & 0 \\ 0 & L_1/T_s \end{bmatrix} \begin{bmatrix} i_{dLP}(k-1) \\ i_{qLP}(k-1) \end{bmatrix} + \begin{bmatrix} -(R_1 + L_1/T_s) & \omega_{eLP}(k)L_1 \\ -\omega_{eLP}(k)L_1 & -(R_1 + L_1/T_s) \end{bmatrix} \begin{bmatrix} i_{dLP}(k) \\ i_{qLP}(k) \end{bmatrix} \quad (8)$$

where T_s is the sampling period and k is the index of sample.

As mentioned before, the core of seamless transition control is to ensure that the terminal voltages of the LPG remain unchanged before and after any change of the control scheme for the BTB$_1$ converter. Thus, assuming a fault occurs to the LPR in the $(k)_{th}$ sampling interval, a seamless transition requires

$$v_{dLP}(k) = v_{dLP}{}^{ref}(k-1) \quad v_{qLP}(k) = v_{qLP}{}^{ref}(k-1) \quad (9)$$

Using (8) and (9), the BTB$_1$ converter's voltage commands at time $(k)_{th}$, i.e., $v_{dBTB1}(k)$ and $v_{qBTB1}(k)$, can be derived. The implementation of such seamless transient control is shown in **Fig. 11**. Within the digital controller, in each sampling interval, a few events will be implemented in sequence, i.e., fault detection and protection, control scheme application and update the pulse-width modulation (PWM) registers based on the dq-axes voltage commands. At each sampling interval, $v_{dLP}{}^{ref}(k-1)$, $v_{qLP}{}^{ref}(k-1)$, $i_{dLP}(k-1)$, $i_{qLP}(k-1)$, $i_{dLP}(k)$, and $i_{qLP}(k)$ are stored and updated. With the stored values and (9), voltage commands for the BTB$_1$ converter, i.e., $v_{dBTB1}(k)$ and $v_{qBTB1}(k)$, can be calculated using (8). This process is indicated by the star #1 in **Fig. 11**.
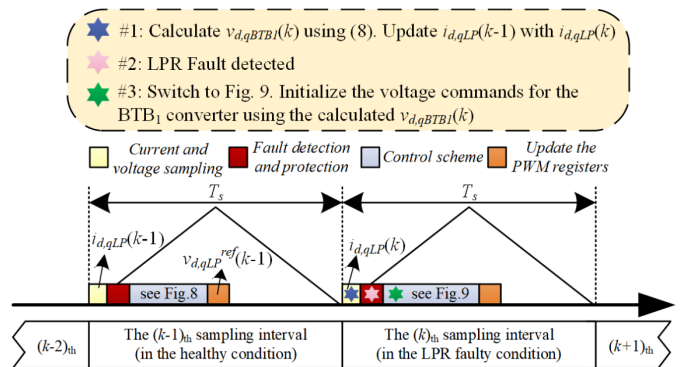

Fig. 11. Schematic diagram of the program execution. The up-down triangle waveform is the time-base counter of PWM module.

Once the fault has been detected and captured by the controller in the $(k)_{th}$ sampling interval, denoted as #2, the system will be reconfigured and the BTB$_1$ converter's control scheme is changed from **Fig. 6** to that in **Fig. 9** within the control scheme application cycle in the #3 process. The voltage commands for the BTB$_1$ converter are set to the calculated $v_{dBTB1}(k)$ and $v_{qBTB1}(k)$ using (8) and (9). Using the revised $v_{dBTB1}(k)$ and $v_{qBTB1}(k)$ to initialize the voltage

commands for the BTB_1 converter will help avoid an abrupt change of the LPG's currents.

From (8) it can be seen that the calculation of the initialization voltage $v_{dBTB1}(k)$ and $v_{qBTB1}(k)$ depends on the value of inductance L_1. Deviation between the actual L_1 (L_1^{act}) and the value used in the digital controller (L_1^{con}) will lead to inaccurate initialization voltages. To study the parameter sensitivity, $v_{dBTB1}(k)$ and $v_{qBTB1}(k)$ at different powers of the LPG and different inductance values used in the digital controller are shown in **Fig. 12**.

In **Fig. 12**, a ±20% inductance mismatch is considered. It can be seen that in the low power region, the mismatch between L_1^{act} and L_1^{con} does not lead to significant deviation in voltages. As the increase of power, $v_{qBTB1}(k)$ with mismatched L_1^{con} is still close to the optimal voltage. But the deviation in $v_{dBTB1}(k)$ becomes significant. Due to the voltage limitation imposed by the dc-link voltage and PWM technique, $v_{dBTB1}(k)$ in the high-power regions is restricted. Hence the optimal initialization voltages cannot be outputted. However, compared with no voltage initialization, in the high-power region the transient performance of the current can still be improved to some extent.
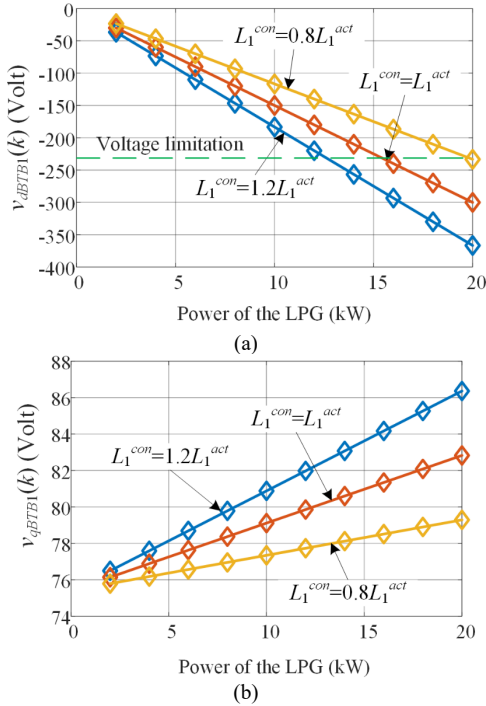

(a)

(b)

Fig. 12. $v_{dBTB1}(k)$ and $v_{qBTB1}(k)$ at different powers of the LPG and different inductance values in controller. Machine parameters of the targeted LPG can be found in [13]. L_1^{act} is the actual inductance of L_1, which is considered as 1mH according to [24]. L_1^{con} is the inductance used in the digital controller.

B. System Reconfiguration and Seamless Transition Scheme Considering the HP Rectifier Failure

In the case of HPR failure, the HPR can be disconnected from the system and the rest of system is reconfigured to a structure shown in **Fig. 13**, where the control schemes for each converter are exhibited. In normal operation conditions, the HPG's power is delivered to the main dc bus through the HPR. In postfault operation conditions, all the HPG's power is transferred to the HVDC bus through the BTB converter and then the LPR converter.

Within this postfault architecture. the LPR is controlled to stabilize the main dc bus voltage. The LPR's inner control loop is a current loop of i_{dLPR} and i_{qLPR}, and the outer loop is to maintain the HVDC bus voltage. The droop control used for power sharing for the LPR is deactivated as the paralleled HPR is unavailable in this scenario.

Since the power flow direction is from the HP to LP channel through the BTB converter, control of the BTB_2 converter is changed to regulate the internal dc-link voltage (which used to be BTB_1 for this function when the LPR fails). As can be seen in **Fig. 13**, where the inner loop of the BTB_2 converter is still the i_{dHP} and i_{qHP} current control, the outer loop is changed to the dc-link voltage v_{BTB} control. For the BTB_1 converter, the phase current synchronization strategy in **Fig. 6** will be used. The gain m is actively managed to control the power from the HPG. The method for controlling m is illustrated as follows.

From the viewpoint of power, the power delivered by the BTB_1 converter from the HP to LP channel essentially comes from the HPG. The LPG's power compensates for the difference between the total load power and the HPG's power. Assuming the targeted power sharing ratio between the LPG and the HPG is $\rho_{LP} : \rho_{HP}$, then the following relation can be derived

$$\frac{3}{2}\left(v_{dBTB1}i_{dBTB1} + v_{qBTB1}i_{qBTB1}\right) = \frac{\rho_{HP}}{\rho_{LP} + \rho_{HP}}P_t \quad (10)$$

where v_{dBTB1} and v_{qBTB1} are the dq-axes voltages of the BTB_1 converter. i_{dBTB1} and i_{qBTB1} are the dq-axes currents of the BTB_1 converter. P_t is the total load power. It can be obtained by the measured dc voltage v_{dc} and load current i_{Load}, where $P_t = v_{dc} \cdot i_{Load}$.

Combining the power sharing ratio equation (2) and (10) it gives

$$\frac{3}{2}m\left(v_{dBTB1}i_{dLP} + v_{qBTB1}i_{qLP}\right) = \frac{\rho_{HP}}{\rho_{LP} + \rho_{HP}}v_{dc}i_{Load} \quad (11)$$
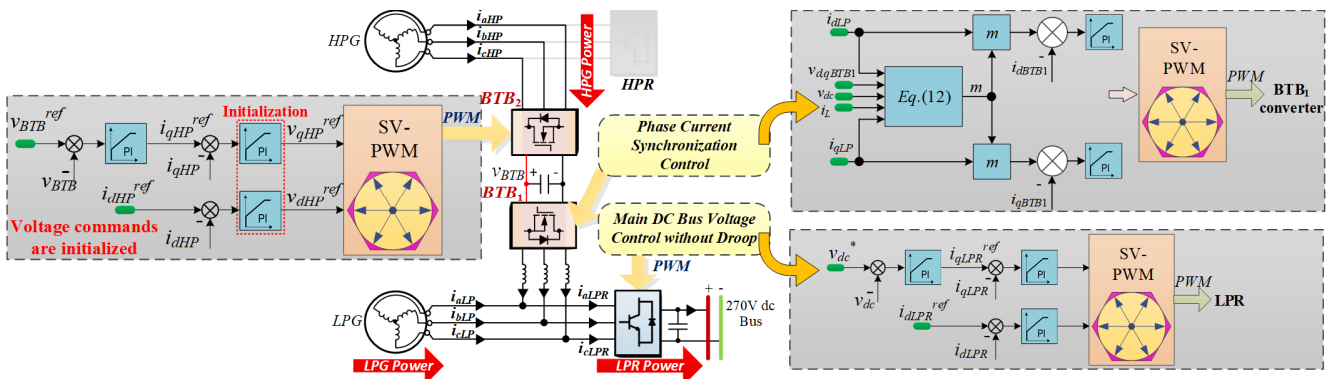

Fig. 13. The power flow diagram and control schemes at HP rectifier fault.

With the defined power ratio ρ_{LP} and ρ_{HP}, the gain m can be calculated as follows:

$$m = \frac{2\rho_{HP}v_{dc}i_L}{3\left(v_{dBTB1}i_{dLP} + v_{qBTB1}i_{qLP}\right)\left(\rho_{LP} + \rho_{HP}\right)} \quad (12)$$

The control scheme for the BTB$_1$ converter under the HPR faulty scenario can thus be given as the structure shown in **Fig. 14**. The functions and control objectives before and after the HPR fault of each converter are presented in **Table III**.
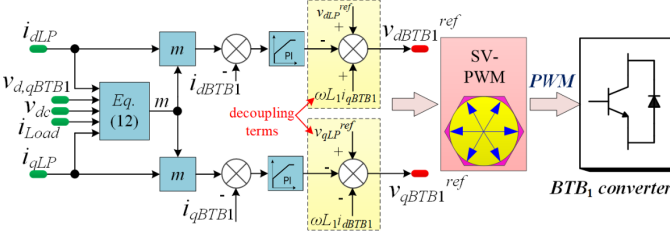

Fig. 14. Control scheme for the BTB$_1$ converter under the HPR faulty scenario.

Table III. Functions and control objectives for each remaining converter when the HPR is disconnected due to fault.

Remaining power converter	Functions	Control objectives	
		Before fault	After fault
LPR	Delivering power to the main dc bus, feeding onboard loads.	Sharing load power under droop control (see **Fig. 4**).	Stabilizing the main dc bus voltage to 270V (see Fig. **13**)
BTB$_1$ converter	Controlling the amount of power drawn from the HPG.	Synchronize the phase currents and stabilize the dc voltage of the BTB converter (see **Fig. 6**)	Managing how much power is extracted from the HPG by controlling the gain m (see Fig. **13**)
BTB$_2$ converter	Providing an additional power flow path to the HPG when the HPR is disconnected.	Controlling the dq-axes currents of the HPG to output power P_{HPG} (see **Fig. 7**)	Stabilizing the internal dc-link voltage within the BTB converter (see Fig. **13**)

As can be seen in **Table III**, the control scheme will be changed for the BTB$_2$ converter before and after the HPR fault. Since the terminals of HPG are directly connected with the BTB$_2$ converter, to avoid the abrupt change of HPG's currents when switching control schemes for the BTB$_2$ converter, the voltage commands in the new control scheme in **Fig. 13** needs to be initialized. Similar to that process after the LPR fault, to achieve a seamless transition before and after the HPR fault, the terminal voltages of the HPG during transition should remain the same. Assuming at $(k-1)_{th}$ interval, voltage commands of the healthy state control scheme in **Fig. 7** are $v_{dHP}^{ref}(k-1)$ and $v_{qHP}^{ref}(k-1)$. At the $(k)_{th}$ sampling interval, a fault occurs to the HPR and it is disconnected from the system. The system is reconfigured to **Fig. 13**. The voltage commands of the new control scheme for the BTB$_2$ converter are initialized as $v_{dHP}^{ref}(k-1)$ and $v_{qHP}^{ref}(k-1)$, respectively.

Comparing the subsections A and B, it can be seen that the difference between the low-side fault tolerance (LFT) and the high-side fault tolerance (HFT) is that the postfault system reconfigurations are different. Hence, the associated fault tolerant controls are also different due to the different reconfigured architectures. The system configuration and

control with LFT is shown in **Fig. 9**, and that with the HFT is shown in **Fig. 13**. Moreover, due to the different locations of the filtering inductance L_1 and L_2 (L_1 is located at the front end of the BTB$_1$ converter and L_2 is located at the front end of the HPR), the seamless transition strategy for the LPG at the low-side failure is different from the seamless transition strategy for the HPG at the high-side failure.

C. Fault Detection

In the following validations, PWM firing pulses for the rectifiers are disabled to simulate the open-circuit fault condition (three-phase open-circuit fault). Since the main objective of this paper is to investigate the postfault reconfiguration and the associated control for the APGC, regarding the fault detection, this paper did not propose a new method. The open-circuit fault detection method proposed in [32] is adopted because it is simple for implementation, fast and accurate for detection, and needless for extra sensors.

The detection logic is straightforward: once a three-phase open-circuit fault occurs, the phase currents drop to zero. This means that after coordinate transformations, the q-axis current i_q^{fdb} is also zero. However, as can be seen in **Fig. 4**, in the digital controller, the output of the dc current controller, which is the reference of q-axis current i_q^{ref} is not zero. If the actual q-axis current i_q^{fdb} is zero whilst the gap between i_q^{ref} and i_q^{fdb} is larger than a defined threshold, the associated rectifier can be considered open circuited. The fault detection process is summarized in the flowchart as shown in **Fig. 15**.
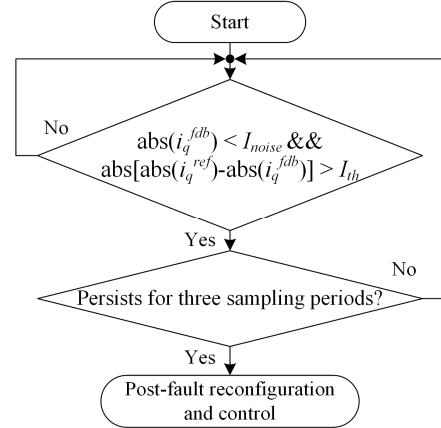

Fig. 15. Flowchart of the open-circuit fault detection method.

In **Fig. 15**, I_{noise} is the noise tolerance for current measurement because even if in the open-circuit condition where the actual i_q^{fdb} is zero, the measured i_q^{fdb} can still have some value due to noises. In this paper I_{noise} is designed as 0.2A. I_{th} is the threshold gap between $abs(i_q^{ref})$ and $abs(i_q^{fdb})$. In this paper I_{th} is set as 50%× $abs(i_q^{fdb})$. If the two conditions are met for more than three consecutive sampling periods, the fault detector will report an open-circuit fault and the system is reconfigured for postfault operation. The maximum detection delay is only three sampling periods. The detection sensitivity can be easily adjusted by tuning I_{noise} and I_{th}.

Although the short-circuit fault scenario is not considered in the following simulation and experiments, the short-circuit detection and isolation technique is briefly presented here for a complete discussion.

The experimental setup uses both hardware protection and software protection to solve the overcurrent problem

caused by the short-circuit faults. The hardware protection is realized by the desaturation function provided by the gate driver IC. The ACPL-331J gate drive output optocoupler is used. ACPL-331J monitors the saturation (collector) voltage of the IGBT and triggers a fault shutdown sequence if the collector voltage exceeds a threshold due to the high short circuit current. Before the dissipated energy can reach destructive levels, the IGBT is shut off. Then the output of pin $\overline{\text{FAULT}}$ (pin No.3) of ACPL-331J is changed from a high impedance state to a logic low state within 5 µs.

From the software side, the output signal from the pin $\overline{\text{FAULT}}$ is measured in every sampling period. If a logic low signal is detected, it means that the desaturation function is triggered due to overcurrent. Then all the PWMs will be disabled in the program of digital signal processor (DSP).

The overall short circuit protection process is summarized in the following flowchart **Fig. 16**, where the software protection and hardware protection are highlighted.
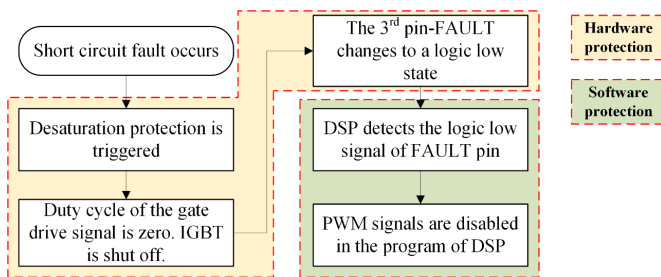

Fig. 16. Flowchart of the short-circuit fault detection and isolation.

IV. Simulation and Experimental Validations

To verify the fault tolerant capability of the APGC and proposed control scheme, a downscaled lab prototype consisting of two rectifiers and one BTB converter has been built as shown in **Fig. 17**. An autotransformer (AF) whose primary side is connected with the utility grid is used to emulate the LPG. The frequency of the AF's voltage is 50Hz. A Chroma QuadTech 31120 programmable ac source is used to emulate the HPG, and its voltage frequency is set as 80Hz. The TMDSCNCD28379D control card is used as the digital control platform. A resistive load bank and an APM electronic load (E-load) are connected to the dc bus. Other system parameters are listed in **Table IV**.

In this section, the system reconfiguration and fault tolerant control proposed in Section III will be investigated in simulation and experiments. Engine performances with the PGC (**Fig. 1**) and the APGC (**Fig. 2**) under the rectifier faulty conditions are also compared using the engine compressor map. The characteristics that will be checked are included in **Table V**.
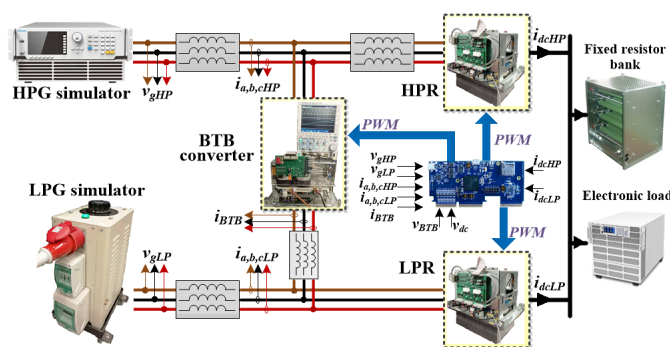

Fig. 17. Configuration of the experimental prototype.

Table IV. Experimental system parameters.

Parameter	Value
Rated dc bus voltage	270 V
Internal dc-link voltage of the BTB converter	400 V
Inductance of the AC filters	2.5 mH
E-load	Constant power load mode
Switching frequency	5 kHz
Current loop and voltage loop execution frequencies	5kHz / 1kHz
Voltage and current Sensors	LV25-P and LA200-P

Table V. The core characteristics and variables that will be checked in simulation and experiment.

Point 1	The main dc bus voltage v_{dc}, and the dc currents of the LPR and HPR, i_{dcLP} and i_{dcHP}. This is used to check the effectiveness of the essential main dc bus voltage control and the droop control in **Fig. 4**.
Point 2	In the case of triggering the open-circuit fault for the LPR, investigating whether system reconfiguration and fault tolerant control in Section III-A can ensure that the two generators continue operating, and all the power is delivered to the dc bus through the remaining HPR. Moreover, during the transition from the healthy state to the postfault operation state, checking whether the LPG's phase current using the voltage command initialization strategy in Section III-A can be smoother than not using the initialization strategy.
Point 3	In the case of triggering the open-circuit fault for the HPR, investigating whether system reconfiguration and fault tolerant control in Section III-B can ensure that the two generators continue operating, and all the power is delivered to the dc bus through the remaining LPR. Moreover, during the transition from the healthy state to the postfault operation state, checking whether the HPG's phase current using the voltage command initialization strategy in Section III-B can be smoother than not using the initialization strategy.
Point 4	Checking whether the power flow of the generators, rectifiers and the BTB converter follows the relation in **Table I**.

A. Simulation Results from the Normal Operation to the LPR Failure

During this simulation study, the APGC starts running under a normal operation condition. A load change is then applied to test the power control in a healthy condition before the LPR failure. The APGC is supplying a 40Ω resistor load through the HVDC bus from the beginning to 1.5s. At t=1.5s, the E-load will be applied and increase the total load power on the dc bus to 3.3kW. At t=2s, PWM signals for the LPR are disabled to simulate the open-circuit faulty scenario for the LPR. Meanwhile, the fault tolerant control is activated. By disabling the PWM signals, the LPR cannot deliver power to the HVDC bus. Hence, the LPR can be regarded as disconnected from the HVDC bus. Currents are normalized into per-unit (pu) where the benchmark current is 35A. For the results in **Fig. 18**, the voltage command initialization for seamless transition is not applied.

The dc bus voltage is presented in **Fig. 18**(a). It can be seen that the HVDC bus voltage v_{dc} deviates from the reference (270V) due to the application of droop control. As the increase of load power at t=1.5s, the deviation becomes larger, and more dc current will be supplied to the HVDC bus from the HPR and LPR. Disabling the PWM signals for the LPR at t=2s, only the HPR is left in the system and there is no need for droop control. Therefore, v_{dc} is restored to the rated value 270V.
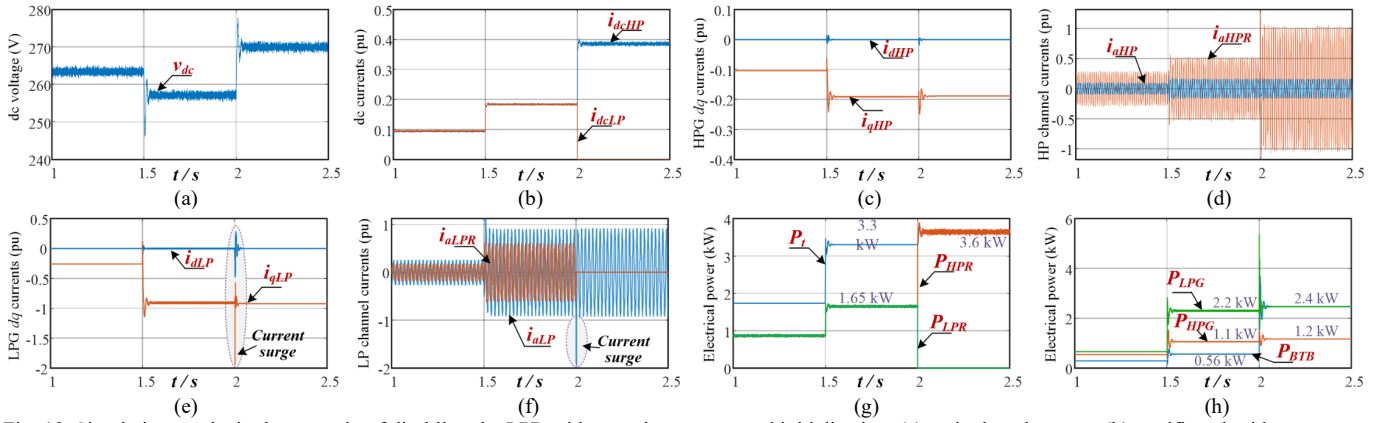
Fig. 18. Simulation results in the scenario of disabling the LPR without voltage command initialization. (a) main dc voltage v_{dc}. (b) rectifiers dc side currents i_{dcLP} and i_{dcHP}. (c) dq currents of the HPG. (d) phase currents of the HPG and HPR. (e) dq currents of the LPG. (f) phase currents of the LPG and LPR. (g) Total load power; output powers of the HPR and LPR. (h) Powers of the LPG, HPG, and BTB converter.

DC currents of the HPR and LPR are shown in **Fig. 18**(b). During this test case, the droop gains of these two converters are set to be identical. As a result, before the fault happens at t=2s, the dc current of the HPR i_{dcHP} equals that of the LPR i_{dcLP}. When disabling the PWM for the LPR at t=2s, the LPR can be regarded as disconnected from the HVDC bus and thus i_{dcLP} is zero. All the power is delivered by the remaining HPR, thus i_{dcHP} doubles from 0.19 pu to around 0.38 pu. Hence, the first point in the checklist **Table V** is validated, confirming the effectiveness of the dc bus voltage control and the droop control in **Fig. 4**.

The dq currents of the HPG and phase currents of the HP channel are exhibited in **Fig. 18**(c) and (d). It can be seen that the d-axis current of the HPG is kept to zero. As the increase of load power at t=1.5s, the magnitude of q-axis current of the HPG also increases. The steady-state values of i_{qHP} during t=1.5s-2s and after t=2s are the same, which means that removal of the LPR does not affect the steady-state operation of the HPG. This can also be observed from the unchanged HPG's phase current i_{aHP}. Since all the power is directed to the HPR, magnitude of the HPR's phase current i_{aHPR} increases significantly after the fault happens t=2s.

dq currents of the LPG and phase currents of the LP channel are exhibited in **Fig. 18**(e) and (f). It can be seen that the phase current of the LPR is zero after t=2s because of the disconnection of the LPR. The steady-state q-axis current and phase current of the LPG are kept unchanged after t=2s. However, since the voltage command initialization for the BTB₁ converter is not considered, current surge occurs in the transient process, which will lead to undesirable torque on the LPG and trigger overcurrent protection of the system. From **Fig. 18**(c)-(f), the second point in **Table V** is validated, confirming that in the case of LPR failure, the system reconfiguration and fault tolerant control in Section III-A can ensure that the two generators continue operating.

Electrical powers of the HPR, LPR, HPG, LPG and total load power are given in **Fig. 18**(g) and (h). Before t=2s, P_{HPR} and P_{LPR} are both 1.65kW due to identical droop gains. At t=2s, PWM signals for the LPR are disabled, hence $P_{LPR}=0$ and $P_{HPR} = P_t$, where P_t is the total load power. The power sharing ratio between the LPG and HPG is set as 2:1. Hence, power of the HPG is one-third of the total power P_t. According to the power relations in Table I, before the fault happens at t=2s, P_{BTB} = HPR Power - HPG Power = $(1/2 - 1/3)P_t = 0.56$kW. After t=2s, the total power increases to

3.6kW as v_{dc} increases to 270V. All the power of the LPG is transferred by the BTB converter, hence, $P_{LPG}=P_{BTB}= 2.4$kW. Hence, the fourth point in **Table V** is validated, confirming that the power flow is consistent with that in **Table I**.

To diminish the current surge during the transition of disabling the LPR, the voltage command initialization strategy proposed in Section III-A is applied and results are shown in **Fig. 19**. It can be seen from the dashed lines in **Fig. 19**(a) that without initialization, the dq voltages of the LPG restore to zero volts at t=2s because of switching to a new control scheme for the BTB₁ converter. The oscillated dq voltages will lead to oscillated currents. This is the reason for the current surge in **Fig. 18**(e) and (f). As a contrast, the solid lines show the dq voltages when the smooth transition scheme is applied after the fault occurs. Consequently, comparing with **Fig. 18**(e) and (f), the currents in **Fig. 19**(b) and (c) transit smoothly with negligible current surge at t=2s. The results confirm the effectiveness of the proposed seamless transition control and thus the second point in the checklist **Table V** is validated.

B. Experimental Results for Cases with the LPR Failure

Experimental results when the LPR fails without seamless transition scheme are presented in **Fig. 20**. There are three operating stages. In stage 1, a fixed resistor is connected to the dc bus, absorbing a 1.2kW power. In stage 2, the E-load performs as a constant power load (CPL), consuming an extra 550W power. In stage 3, the LPR is disconnected to simulate the faulty scenario. The droop gains for the HPR and LPR are set identical in the first two stages.

From **Fig. 20**(a) it can be seen that i_{dcLP} and i_{dcHP} are the same in the first two stages due to identical droop gains. The dc bus voltage v_{dc} decreases from 268V in stage 1 to 265V in stage 2 because of increased power. After disabling the PWM for the LPR, i_{dcLP} drops to zero, while i_{dcHP} is around double from 3.3A to 6.4A because the HPR delivers all of the load power. v_{dc} restores to the rated 270V in stage 3 as only the HPR is left hence there is no need for power sharing using droop control. The results in **Fig. 20**(a) are perfectly consistent with the simulation results in **Fig. 18**(a) and (b).

The experimental results of phase currents are exhibited in **Fig. 20**(b). With the increase of power from 1.2kW to 1.75kW, the magnitude of all phase currents also increases. After disabling the PWM for the LPR, i_{aLPR} becomes zero, while i_{aHPR} boosts because the HPR carries all the load power.
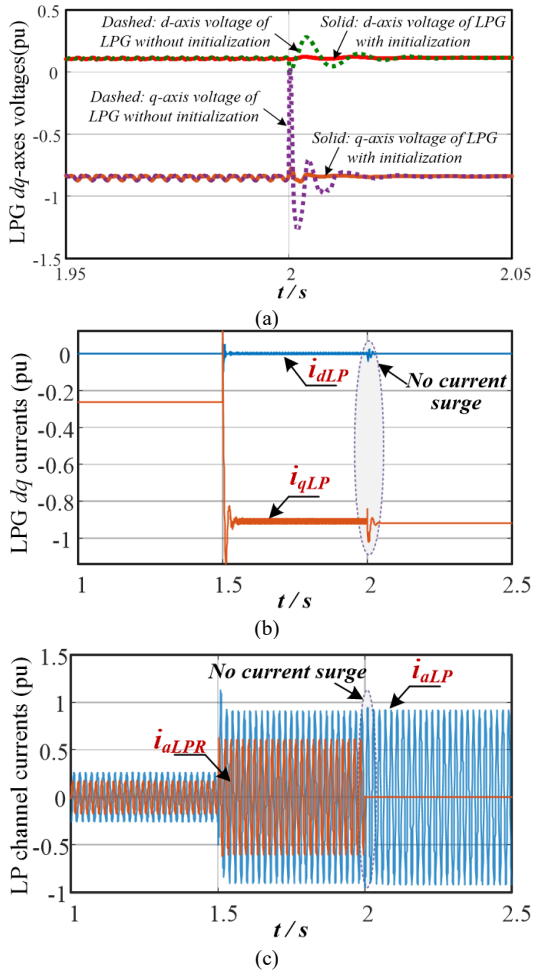
10

Fig. 19. Simulation results with voltage command initialization. (a) comparison of *dq* voltages of LPG with and without voltage command initialization. (b) *dq* currents of LPG with initialization. (c) phase currents of LPG and LPR with initialization.
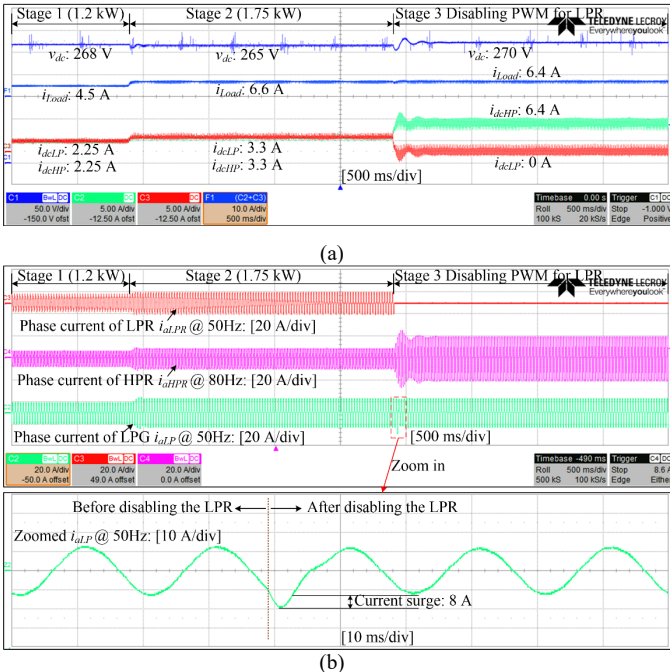

Fig. 20. Experimental results of disabling the LPR without voltage command initialization. (a) main dc voltage v_{dc}, rectifiers dc side currents i_{dcLP} and i_{dcHP}, and total load current i_{Load}. (b) phase currents of HPR, LPR, and LPG, and expanded figure of LPG's phase current.
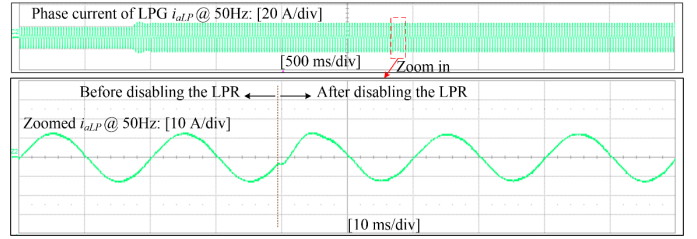

Fig. 21. Experimental results in the scenario of disabling the LPR with the proposed voltage command initialization.

Evident current surge in the LPG's phase current i_{aLP} can be seen in the transient process of the LPR's disconnection. As can be seen in the expanded figure, the current surge is around 8A larger than the normal phase current. Te results in **Fig. 20**(b) are in accordance with the simulation results in **Fig. 18**(d) and (f).

To diminish the current surge in the LPG's phase current, the proposed voltage command initialization strategy is used as shown in **Fig. 21**. Compared with **Fig. 20**(b), the proposed method provides a much smoother transient performance in i_{aLP}. Overall, the results in **Fig. 20** and **Fig. 21** confirm the fault tolerance improvement and seamless transition when the LPR fails.

C. Simulation Results from the Normal Operation to the HPR Failure

Simulation results when the HPR's failure occurs are demonstrated in **Fig. 22**. In stage 1, t=1s-1.5s, the dc bus is loaded with a 40Ω resistor. In stage 2, t=1.5s-2s, the load power increases to 3.3kW. Stage 3: at t=2s, PWMs for the HPR are disabled.

The performance of the main dc bus voltage in **Fig. 22**(a) is the same as that in **Fig. 18**(a). For the dc currents demonstrated in **Fig. 22**(b), since the two droop gains are identical, hence before t=2s, $i_{dcHP} = i_{dcLP}$. At t=2s, i_{dcHP} changes to zero because the gate drive signals for the HPR are disabled, which means that the HPR can be regarded as disconnected from the HVDC bus. Hence, the first point in the checklist **Table V** is validated, proving the effectiveness of the dc bus voltage control and the droop control in **Fig. 4**.

The *dq* currents of the HPG and phase currents of the HP channel are presented in **Fig. 22**(c) and (d). It can be seen that the phase current of the HPR, i_{aHPR}, is zero after t=2s due to disabling the HPR. The values of other currents are kept unchanged after the HPR fails, which means that the operation of the HPG is not affected. However, since the voltage command initialization for the BTB₂ converter is not considered, the current surge of the HPG can be observed in the transient process.

dq currents of the LPG and phase currents of the LP channel are exhibited in **Fig. 22**(e) and (f). From **Fig. 22**(e) it can be concluded that operation of the LPG stays the same as that in the healthy state. **Fig. 22**(f) shows that before t=2s, the magnitude of i_{aLPR} is smaller than i_{aLP} because the BTB converter transfers power from the LP to HP channel. However, after t=2s, the HPG outputs power to the LP channel through the BTB converter, making the magnitude of i_{aLPR} larger than that of i_{aLP}. From **Fig. 22**(c)-(f), the third point in the checklist **Table V** is validated, confirming that in the case of the HPR failure, the system reconfiguration and fault tolerant control in Section III-B can ensure that the two generators continue operating as normal.
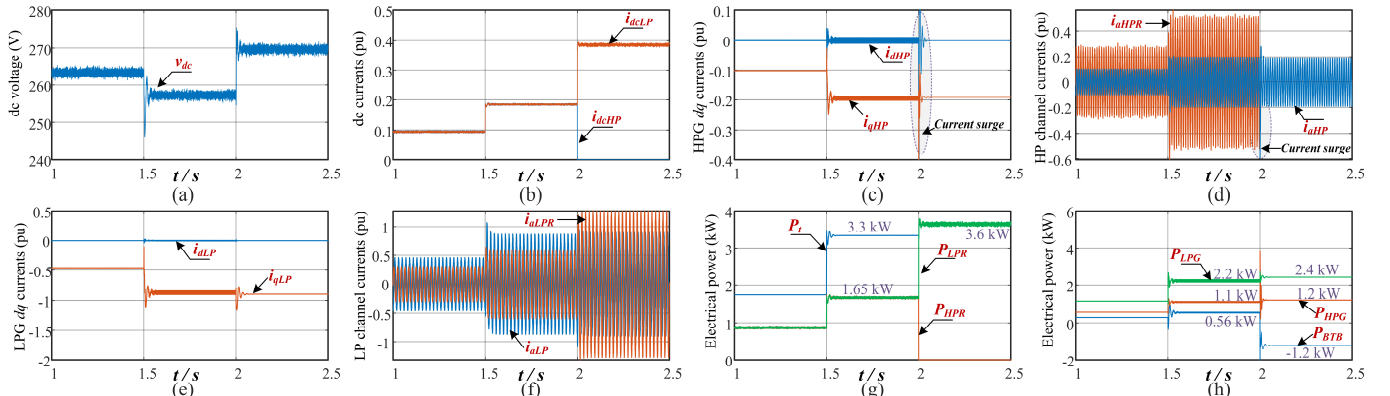
Fig. 22. Simulation results in the scenario of disabling the HPR without voltage command initialization. (a) main dc voltage v_{dc}. (b) rectifiers dc side currents i_{dcLP} and i_{dcHP}. (c) dq currents of HPG. (d) phase currents of HPG and HPR. (e) dq currents of LPG. (f) phase currents of LPG and LPR. (g) Total load power; output powers of HPR and LPR. (h) Powers of LPG, HPG, and BTB converter.

Electrical powers are given in **Fig. 22**(g) and (h). Before t=2s, P_{HPR} and P_{LPR} are 1.65kW, achieving an equal power sharing. At t=2s, gate drive signals for the HPR are disabled, hence P_{HPR} =0 and $P_{LPR} = P_t$ = 3.6kW. The power sharing ratio between the LPG and HPG is set as 2:1. Hence, the power of the HPG is one-third of the total power P_t. The BTB converter carries all 1.2kW power of the HPG. A negative power P_{BTB} shows that this power is transferred from the HP to the LP channel. Hence, the fourth point in the checklist **Table V** is validated, confirming that the power flow is consistent with that in **Table I**.

The voltage command initialization strategy proposed in Section III-B is tested to limit the current surge in the transition of disabling the HPR. As can be seen from the dashed lines in **Fig. 23**(a), without initialization, dq voltages of the HPG change to zero volts at t=2s and then oscillate because a new control scheme is applied to the BTB$_2$ converter. The oscillated voltages lead to current surge in **Fig. 22**(c) and (d). However, with the voltage initialization, voltages of the HPG transit smoothly at t=2s. Therefore, **Fig. 23**(b) and (c) show a much smoother current performance than that in **Fig. 22**(c) and (d). This means that the voltage initialization method in Section III-B can effectively ensure a smooth transition, and hence the third point in **Table V** is validated.

D. Experimental Results for Cases with the HPR Failure

Experimental results of the HPR failure without voltage command initialization are given in **Fig. 24**. The operating stages and settings are the same as that in **Fig. 20**. From **Fig. 24**(a) it can be seen that the dc currents are the same in the first two stages due to identical droop gains. The dc bus voltage drops with the increase of power. In stage 3 where the PWM signals for the HPR are disabled, i_{dcHP} falls to zero and i_{dcLP} is doubled. The dc bus voltage restores to 270V because of the deactivation of droop control. The results in **Fig. 24**(a) are consistent with the simulation results in **Fig. 22**(a) and (b).

The experimental results of phase currents are shown in **Fig. 24**(b). As the load power increases from 1.2kW to 1.75kW, the magnitude of all phase currents also increases. In the transient process when the PWM signals for the HPR are disabled, i_{aHPR} drops to zero, and i_{aLPR} boosts significantly. Current surge of i_{aHP} is highlighted in a dash rectangular. A 16A current surge can be seen in the expanded figure. The results in **Fig. 24**(b) are consistent with the simulation results

in **Fig. 22**(d) and (f), showing that phase current surge will occur to the HPG if directly changing to the fault tolerant control without voltage command initialization.
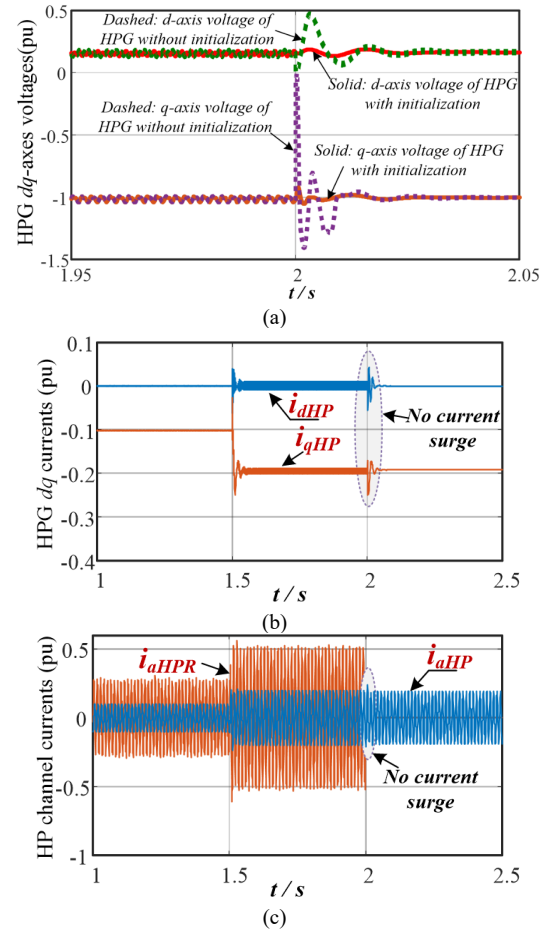

Fig. 23. Simulation results with voltage command initialization. (a) comparison of dq voltages of HPG with and without voltage command initialization. (b) dq currents of HPG with initialization. (c) phase currents of HPG and HPR with initialization.

The effectiveness of the proposed voltage command initialization strategy is tested as shown in **Fig. 25**. Compared with **Fig. 24**(b), the transient performances of the HPG's phase current become smoother with limited current surge and recovery time. This is consistent with the simulation results shown in **Fig. 23**, confirming that the proposed voltage command initialization strategy can provide a seamless transition when disabling the HPR.
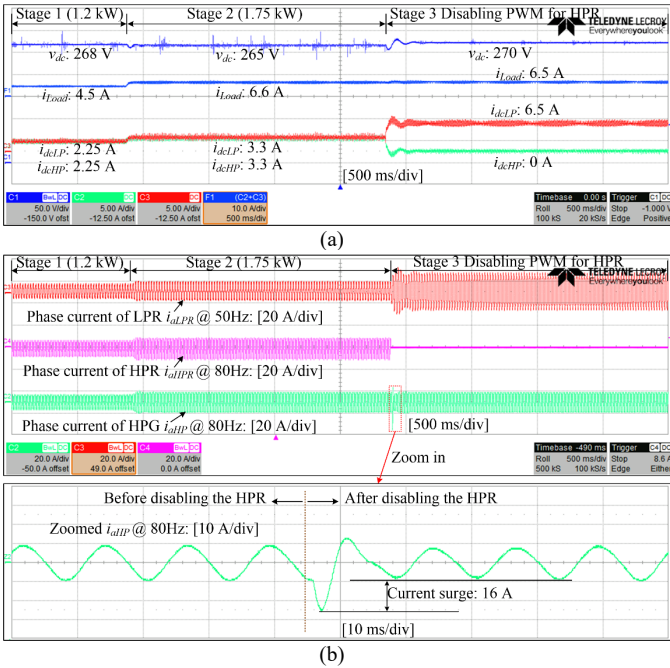
(a)

(b)

Fig. 24. Experimental results of disabling the HPR without voltage command initialization. (a) main dc voltage v_{dc}, rectifiers dc side currents i_{dcLP} and i_{dcHP}, and total load current i_{Load}. (b) phase currents of HPR, LPR, and HPG, and expanded figure of HPG's phase current.
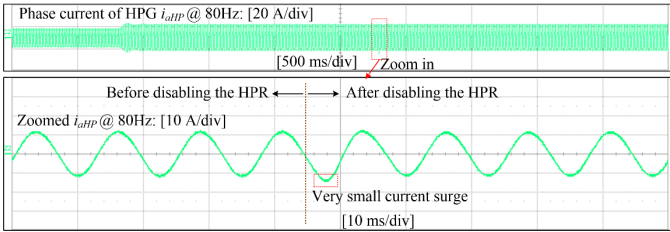

Fig. 25. Experimental results in the scenario of disabling the HPR with the proposed voltage command initialization.

E. Engine Performance Comparison using Different Power Generation Center Architectures

To study the engine performances with the PGC in **Fig. 1** and the APGC in **Fig. 2**, a multi-spool turbofan model has been developed by our group using the intercomponent volume method and CFM56 engine maps [2], [28]. The cruise mode is focused because cruising usually consumes the majority of a flight. The altitude is 39kft, Mach number is 0.79. The speed of the LPS is fixed to provide a constant thrust. The operating points are shown in **Fig. 26**, where A and B indicate that the engine operates with the PGC in **Fig. 1** and the APGC in **Fig. 2**. LPR is consdiered faulty and disconnected from the system.

As proved in the previous subsections, with the APGC, operating states of the LPG and HPG are not affected when disabling the LPR. However, with the PGC, disabling the LPR will make the remnant HPR feed all the load power. As a result, the HPG needs to extract more mechanical power from the HPS, decreasing the rotary speed of the HPS. Since the high-pressure compressor (HPC) is coupled with the HPS, the speed of the HPC is also reduced, leading to a decreased mass flow demand. In this case, the HPC acts as a blockage for the rear side of the low-pressure compressor (LPC), pushing the LPC to decrease its mass flow at the same speed. Consequently, the pressure ratio of the LPC will increase and the operating point will move close to the surge line on the

compressor map. This is the reason why the operating points in **Fig. 26** move from B to A.
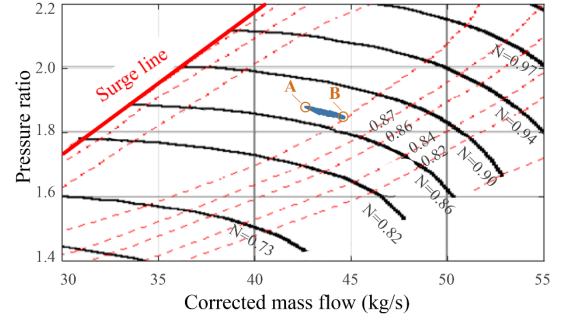

Fig. 26. Low-pressure compressor map and operating points in the cruise mode (39kft, Mach=0.79).

Comparing point B with A, it can be concluded that when the LPR is faulty and disconnected, the APGC can provide a larger compressor surge margin than the PGC does. A larger surge margin means a larger stability margin. Therefore, the APGC is a favorable option considering the safe operation of engine.

V. Considerations of the APGC in Practical Application

A. System Weight and Fuel Efficiency Analysis

Compared with the PGC in **Fig. 1**, there is an additional BTB converter (including two AC/DC power converters), capacitor bank, and filtering inductors in the APGC in **Fig. 2**. These components bring extra weight and size, which will cost more fuel burn. However, as revealed in [24], the APGC offers a higher power generation efficiency than the PGC. This subsection will investigate how the actual fuel efficiency will change with the APGC architecture.

A1. Fuel Consumption Increase due to the Additional Back-to-back Converter System

The B787 Dreamliner is considered as the targeted MEA. The essential characteristic of the B787 is listed in **Table VI**. It can be seen that the total power rating of the main generators is 1000 kVA. For the state-of-the-art power electronics technologies, the power density is considered as 14.3 kW/kg and the power conversion efficiency is 97.5% [33], [34]. Hence, given the requirement to handle the 1000kVA power in the postfault operation mode, the weight of the power electronics of the BTB converter can be assumed to be: $W_{PE} = W_{BTBL} + W_{BTBH} = 2\times[1000kW/(97.5\%\times14.3 \ kW/kg)] = 143.3$ kg. The power density of the cooling system is considered as 15 kW/kg [35], hence the weight can be assumed to be $W_{Cool} = 2\times(1000kW/15 \ kW/kg) = 133.3$ kg. Some state-of-the-art inductors for high-current high-frequency applications with acceptable weight ($W_L = 23.5$kg [36]) are suitable to be applied in the APGC. Hence the total weight increase is $W_{Total} = W_{PE} + W_{Cool} + 2\times2\times W_L = 370.6$ kg.

A rule-of-thumb is that an 1% increase in weight results in an 0.75% increase in fuel consumption (FC) [37]. Considering the maximum landing weight in **Table VI** and the total FC of a typical 4-hour flight mission using the CFM56-3 engine in **Table VII** [2], the extra FC due to added weight is:

$$\text{Extra FC} = \frac{W_{Total}}{201,000\text{kg}} \times \frac{0.75\%}{1\%} \times 3964\text{kg} = 5.5 \text{ kg} \quad (13)$$

13

Table VI. Characteristic of the B787.

Parameter	Value	Parameter	Value
Number of engines	2	Power rating of the generators in each engine	2×250 kVA
Maximum landing weight	201,000 kg	Aviation fuel energy density	12.5 kW·h/kg

Table VII. Average fuel consumption of a CFM56-3 engine for a 4-hour flight mission [2].

Flight phase	Time	FC per unit time	Total FC
Taxiing	5 min	9.9 kg/min	49.5 kg
Climb	30 min	42.11 kg/min	1263.3 kg
Cruise	180 min	13.39 kg/min	2410.2 kg
Descent	25 min	7.66 kg/min	191.5 kg
Taxiing	5 min	9.9 kg/min	49.5 kg
Total flight mission	245 min	-	3964 kg

A2. Fuel Consumption Decrease due to the Higher Power Generation Efficiency

As indicated in [24], a 5% power generation efficiency improvement can be achieved using the APGC compared with the PGC. Therefore, the total energy saving with the APGC can be calculated with the flight mission data in **Table VII**:

$$Energy\ saving = 1000kW \times 5\% \times 245\,min / 60\,min / h$$
$$= 204kW \cdot h \qquad (14)$$

Considering the aviation fuel energy density in **Table VI**, the saved FC is 204 kW·h/12.5 kW·h/kg = 16.32 kg. Consequently, the saved FC (16.32 kg) is larger than the extra consumed FC (5.5 kg), which means a higher fuel efficiency is achieved by using the APGC architecture for the studied B787 aircraft in a 4-hour flight mission scenario.

B. Potential Challenges from the Down-scale Lab Prototype to a Full-scale System

Although the effectiveness of the postfault reconfiguration and fault tolerant control has been verified in this paper, there are still some challenges in implementing the proposed method to a full-scale system. The potential challenges include:

- The scaling of essential variables such as the generator's speed and torque used for feedback control.
- To investigate the dynamic performance of a full-scale system through an available down-scale system, time should be scaled as well.

Moreover, in the lab prototype an autotransformer and a programable ac source are used as the LPG and HPG simulator, respectively. There are some differences between the generator simulators and the actual generators. To be specific:

- The actual generators have shaft inertia while the generator simulators do not. The shaft inertia determines the rate of change of speed, which correlates to the back EMF and fundamental frequency of the actual generators. As a contrast, for the generator simulator, there is no back EMF, and the fundamental frequency is manually changed.
- Another difference is related to the control issues. For an electrical generator for high-speed applications, the electrical parameters are relatively small. For example,

for the AEGART electrical machine developed under the frame of the Clean Sky project [26], the stator resistance and inductance are 1.058 mΩ and 100 μH, respectively [38]. Such a small impedance causes the motor current to change quickly, resulting in difficulty for discrete digital control. Moreover, the machine parameters depend on operating conditions, such as stator current, fundamental frequency, and temperature [39]. All these issues cause difficulty in control. As a contrast, these nonlinearities do not exist in the generator simulator, which ease the control design.

Although there are some differences between the actual system and the lab prototype, from the perspective of fault-tolerant control and power control that this paper focuses, these differences do not cause significant impact. The idea of system reconfiguration and fault tolerant control strategy are the same, while the control parameters and control bandwidth should be adjusted for a larger scale system.

VI. Conclusion

To reduce the power losses caused by the significant field-weakening current of the HPG, and enhance fault tolerance of the power generation system in the more-electric aircraft, an advanced power generation center (APGC) was proposed in our previous work. As a continuation, to fully exploit the APGC's fault tolerance potential, in this paper, system reconfiguration and associated fault tolerant control is tailored for the APGC. The main advantages of the proposed solution that have been experimentally and simulatively validated can be highlighted as follows:

- After the HPR or LPR failure, through system reconfiguration and fault tolerant control, the BTB converter can provide a power flow path to the generator of the failed channel. The generator associated with the faulty rectifier can supply continuous power through the BTB converter to the healthy rectifier and then to the dc bus. In this way, the generator can provide power to the load without interruption, which ensures a reliable power supply capability and this is proved beneficial to the stability of the engine.
- To avoid the current surge of the generator's current during the transition from the normal operation to postfault operation, a seamless transition strategy is proposed where the voltage command is properly initialized when switching to a new controller of the BTB converter.

Overall, this paper provided a systematic solution of the fault tolerance enhancement for the APGC. The proposed strategy of system reconfiguration and seamless transition can be of interest for other researchers who are interested in the fault tolerance issue of the onboard dc grid of the MEA.

Besides the field-weakening current elimination and fault tolerance enhancement, the APGC is found to have the potential to improve stability of both dc grid and engine. At the high-power settings of engine, more mechanical power can be taken from the HP spool than LP spool to avoid overspeed of the HP spool. However, by analyzing the stability of the dc grid, it reveals that the LPR should share more power that the HPR. Denoting the power of the HP spool, LP spool, HPR and LPR as P_{HPS}, P_{LPS}, P_{HPR} and P_{LPR}. For the PGC in **Fig. 1**, if $P_{HPS} > P_{LPS}$, P_{LPR} cannot be larger than P_{HPR}. Otherwise, if $P_{LPR} > P_{HPR}$, P_{HPS} cannot be larger

than P_{LPS}. Hence, PGC is hard to improve both engine and dc grid stability. But the APGC in **Fig. 2** can fulfill this goal by transferring power from the HP to LP channel through the BTB converter channel. Detailed study regarding this point is currently under development by our team.

Acknowledgement

References

[1] V. Madonna, P. Giangrande and M. Galea, "Electrical Power Generation in Aircraft: Review, Challenges, and Opportunities," *IEEE Trans. Transport. Electrific.*, vol. 4, no. 3, pp. 646-659, Sept. 2018.

[2] H. B. Enalou, X. Lang, M. Rashed and S. Bozhko, "Time-Scaled Emulation of Electric Power Transfer in the More Electric Engine," *IEEE Trans. Transport. Electrific.*, vol. 6, no. 4, pp. 1679-1694, Dec. 2020.

[3] G. C. Lemmers, Jr. and D. S. Behling, "High to low pressure shaft summing gearbox for accessory power extraction and electric start," *U.S. Patent* 7 882 691, Feb. 8, 2011.

[4] F. Gao, S. Bozhko, G. Asher, P. Wheeler and C. Patel, "An Improved Voltage Compensation Approach in a Droop-Controlled DC Power System for the More Electric Aircraft," *IEEE Trans. Power Electron.*, vol. 31, no. 10, pp. 7369-7383, Oct. 2016.

[5] F. Bu, H. Liu, W. Huang, Y. Hu, M. Degano, C. Gerada, and K. Rajashekara, ''Induction-machine-based starter/generator systems: Techniques, developments, and advances,'' *IEEE Ind. Electron. Mag.*, vol. 14, no. 1, pp. 4–19, Mar. 2020.

[6] Y. Jia and K. Rajashekara, "An Induction Generator-Based AC/DC Hybrid Electric Power Generation System for More Electric Aircraft," *IEEE Trans. Indus. Appl.*, vol. 53, no. 3, pp. 2485-2494, June 2017.

[7] C. Wang, T. Yang, P. Kulsangcharoen and S. Bozhko, "An Enhanced Second Carrier Harmonic Cancellation Technique for Dual-Channel Enhanced Power Generation Centre Applications in More-Electric Aircraft," *IEEE Trans. Indus. Electron*, vol. 68, no. 7, pp. 5683-5692, July 2021.

[8] K. Ni *et al*., "Electrical and Electronic Technologies in More-Electric Aircraft: A Review," *IEEE Access*, vol. 7, pp. 76145-76166, 2019.

[9] L. Chen *et. al.*, "Predictive Control Based DC Microgrid Stabilization With the Dual Active Bridge Converter," *IEEE Trans. Indus. Electron.*, vol. 67, no. 10, pp. 8944-8956, Oct. 2020.

[10] C. Li *et al*., "A Modified Neutral Point Balancing Space Vector Modulation for Three-Level Neutral Point Clamped Converters in High-Speed Drives," *IEEE Trans Ind. Electron.*, vol. 66, no. 2, pp. 910-921, Feb. 2019.

[11] G. Buticchi, S. Bozhko, M. Liserre, P. Wheeler and K. Al-Haddad, "On-Board Microgrids for the More Electric Aircraft—Technology Review," *IEEE Trans Indus. Electron.*, vol. 66, no. 7, pp. 5588-5599, July 2019.

[12] *Aircraft Electric Power Characteristics*, American Military Std. MILSTD-704F, Mar. 2004.

[13] S. Bozhko, M. Rashed, C. I. Hill, S. S. Yeoh and T. Yang, "Flux-Weakening Control of Electric Starter–Generator Based on Permanent-Magnet Machine," *IEEE Trans. Transport. Electrific.*, vol. 3, no. 4, pp. 864-877, Dec. 2017.

[14] K. Hu, Z. Liu, Y. Yang, F. Iannuzzo and F. Blaabjerg, "Ensuring a Reliable Operation of Two-Level IGBT-Based Power Converters: A Review of Monitoring and Fault-Tolerant Approaches," *IEEE Access*, vol. 8, pp. 89988-90022, 2020.

[15] K. Fischer *et al*., "Field-Experience based root-cause analysis of powerconverter failure in wind turbines," *IEEE Trans. Power Electron.*, vol. 30, no. 5, pp. 2481–2492, May 2015.

[16] K. Ni, Y. Hu, G. Chen, C. Gan and X. Li, "Fault-Tolerant Operation of DFIG-WT With Four-Switch Three-Phase Grid-Side Converter by Using Simplified SVPWM Technique and Compensation Schemes," *IEEE Trans. Indus. Appl.*, vol. 55, no. 1, pp. 659-669, Jan.-Feb. 2019.

[17] J. S. Lee and K. B. Lee, "Open-Switch Fault Tolerance Control for a Three-Level NPC/T-Type Rectifier in Wind Turbine Systems," *IEEE Trans. Industrial Electron.*, vol. 62, no. 2, pp. 1012-1021, Feb. 2015.

[18] A. Kersten *et al.*, "Fault Detection and Localization for Limp Home Functionality of Three-Level NPC Inverters With Connected Neutral

[19] J. Zhang, L. Hu, S. Xu, and F. Deng. "Fault-tolerant compensation control for T-type three-level inverter with zero-sequence voltage injection." *IET Power Electronics*, no. 14, pp. 3774-3781, 2019.

[20] F. Chai, L. Gao, Y. Yu and Y. Liu, "Fault-Tolerant Control of Modular Permanent Magnet Synchronous Motor Under Open-Circuit Faults," *IEEE Access*, vol. 7, pp. 154008-154017, 2019.

[21] R. R. Errabelli and P. Mutschler, "Fault-tolerant voltage source inverter for permanent magnet drives," *IEEE Trans. Power Electron.*, vol. 27, no. 2, pp. 500–508, Feb. 2012.

[22] G. Chen and X. Cai, "Reconfigurable control for fault-tolerant of parallel converters in PMSG wind energy conversion system," *IEEE Trans. Sustain. Energy*, vol. 10, no. 2, pp. 604–614, Apr. 2019.

[23] X. Zhang, T. Wang, X. Wang, G. Wang, Z. Chen, and D. Xu, "A coordinate control strategy for circulating current suppression in multiparalleled three-phase inverters," *IEEE Trans. Ind. Electron.*, vol. 64, no. 1, pp. 838–847, Jan. 2017.

[24] X. Lang, *et al.*, "A Dual-Channel-Enhanced Power Generation Architecture With Back-to-Back Converter for MEA Application," *IEEE Trans. Indus. Appl.*, vol. 56, no. 3, pp. 3006-3019, May-June 2020.

[25] X. Lang, T. Yang, H. B. Enalou, C. Li, S. Bozhko, and P. Wheeler, "A dual-channel enhanced power generation architecture with back-to-back converter for MEA application," in *Proc. IEEE Int. Electr. Mach. Drives Conf.*, San Diego, CA, USA, May 2019, pp. 1392–1397.

[26] *Final Report Summary - AEGART (AIRCRAFT ELECTRICAL GENERATION SYSTEM WITH ACTIVE RECTIFICATION AND HEALTH MONITORING).* Accessed: Apr. 2021. [Online]. Available: https://cordis.europa.eu/project/id/296090/reporting.

[27] J. M. Guerrero, M. Chandorkar, T.-L. Lee, and P. C. Loh, "Advanced control architectures for intelligent microgrids–Part I: Decentralized and hierarchical control,*" IEEE Trans. Ind. Electron.,* vol. 60, no. 4, pp. 1254– 1262, Apr. 2013.

[28] H. B. Enalou, S. Bozhko, M. Rashed, and J. Le-Peuvedic, "Potential improvements in turbofan's performance by electric power transfer,*" SAE Tech. Paper,* 2018-01-1962, 2018.

[29] S. Kim, Y. Jang and R. Kim, "Modeling and Hierarchical Structure Based Model Predictive Control of Cascaded Flying Capacitor Bridge Multilevel Converter for Active Front-End Rectifier in Solid-State Transformer," *IEEE Trans. Indus. Electron.*, vol. 66, no. 8, pp. 6560-6569, Aug. 2019.

[30] R. Basak, and *et. al.*, "Low-Voltage Ride-Through of a Synchronous Generator-Based Variable Speed Grid-Interfaced Wind Energy Conversion System," *IEEE Trans. Indus. Appl.*, vol. 56, no. 1, pp. 752-762, Jan.-Feb. 2020.

[31] L. Qu, W. Qiao and L. Qu, "An Extended-State-Observer-Based Sliding-Mode Speed Control for Permanent-Magnet Synchronous Motors," " *IEEE J. Emerg. Sel. Topics Power Electron.*, vol. 9, no. 2, pp. 1605-1613, April 2021.

[32] Z. Wen, G. Valente, A. Formentini, L. Papini, C. Gerada and P. Zanchetta, "Open Circuit Fault Control Techniques for Bearingless Multi-Sector Permanent Magnet Synchronous Machines," *IEEE Trans. Indus. Appl.*, doi: 10.1109/TIA.2021.3060368.

[33] Sahoo, S., Zhao, X., and Kyprianidis, K., 2020, "A Review of Concepts, Benefits, and Challenges for Future Electrical Propulsion-Based Aircraft," *Aerospace*, 7(4), p. 44.

[34] N. Swaminathan and Y. Cao, "An Overview of High-Conversion High-Voltage DC–DC Converters for Electrified Aviation Power Distribution System," *IEEE Trans. Transport. Electrific.*, vol. 6, no. 4, pp. 1740-1754, Dec. 2020.

[35] Balaghi Enalou, Hossein, and Serhiy Bozhko. "Electric Power Transfer Concept for Enhanced Performance of the More Electric Engine." *Journal of Engineering for Gas Turbines and Power*, 143.9 (2021): 091002.

[36] *HCS-601M-500AG inductor.* Accessed: May. 2021. [Online]. Available https://www.coilws.com/images/HCS-601M-500AG%20REV.A.pdf.

[37] H. B. Enalou and S. Bozhko, "Performance improvement of turbofans by electric power transfer", *ASME J. Turbomachinery*, Jun. 2020.

[38] A. M. Diab, S. Bozhko, M. Galea and C. Gerada, "Stable and Robust Design of Active Disturbance-Rejection Current Controller for Permanent Magnet Machines in Transportation Systems," *IEEE Trans. Transport. Electrific.*, vol. 6, no. 4, pp. 1421-1433, Dec. 2020.

[39] X. Lang, *et. al.*, "An Enhanced Feedforward Flux Weakening Control for High-Speed Permanent Magnet Machine Drive Applications", *IET Power Electronics*, in press.

Xiaoyu Lang received the B.S. degree and M.Sc. degree with Honors in electrical engineering from the Harbin Institute of Technology (HIT), Harbin, China, in 2015 and 2017, respectively. He is currently working towards the Ph.D degree at the Power Electronics, Machines and Control Group, The University of Nottingham, Nottingham, NG7 2RD, U.K. His research interests include high speed machine drives, advanced integrated power generation center for more electric aircrafts, and DC microgrid stability.
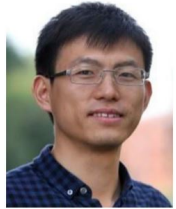
Tao Yang (M'16–SM'20) received the Ph.D. degree in electrical engineering from the University of Nottingham, Nottingham, U.K., in 2013.

Since then, he has been a Researcher and an Associate Professor with the Power Electronics, Machines and Control Group, University of Nottingham. His research interests include aircraft electrical power systems and high-speed motor drives for aerospace applications.

Zhenyu Wang received the B.S. degree in Electrical Engineering, from Chongqing University, Chongqing, China in 2012, and the M.S. and Ph.D. degree in Power Electronics from the University of Nottingham, Nottingham, UK, in 2014 and 2018, respectively.

He is currently a Research Fellow with the Power Electronics, Machines and Control (PEMC) Group at the University of Nottingham, Nottingham, UK. He was a visiting scholar with the LEMUR Research Group at the University of Oviedo, Spain, from April 2016 to February 2017. His Research interests include SiC and GaN devices and applications, DC-DC converters for marine and aerospace applications, magnetic components for power electronic converters and power converter control.
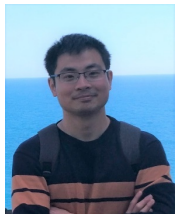
Cheng Wang was born in Jiangsu, China. He received the B.Eng. and M.Sc. degrees in electrical engineering from Nanjing University of Aeronautics and Astronautics, Nanjing, China, in 2013 and 2016, respectively. Since 2017, he is currently working toward the Ph.D. degree in electrical and electronic engineering with the Power Electronics, Machines, and Control Group, University of Nottingham, Nottingham, U.K. His research interests include control and power quality improvement in area of electric DC power systems.

Serhiy Bozhko (M'96–SM'18) received his M.Sc. and Ph.D. degrees in electromechanical systems from the National Technical University of Ukraine, Kyiv City, Ukraine, in 1987 and 1994, respectively.

Since 2000, he has been with the Power Electronics, Machines and Controls Research Group of the University of Nottingham, United Kingdom, where currently he is Professor of Aircraft Electric Power Systems and Director of the Institute for Aerospace Technology. He is leading several EU- and industry funded projects in the area of aircraft electric power systems, including power generation, distribution and conversion, power quality, control and stability issues, power management and optimization, as well as advanced modeling and simulations methods.

Patrick Wheeler (Fellow, IEEE) received the B.Eng. (hons.) degree in electrical engineering and the Ph.D. degree for his work on matrix converters from the University of Bristol, Bristol, U.K., in 1990 and 1994, respectively.

In 1993, he moved to the University of Nottingham, Nottingham, U.K., where he worked as a Research Assistant with the Department of Electrical and Electronic Engineering. In 1996, he became a Lecturer with the Power Electronics, Machines and Control Group, University of Nottingham, where he has been a Full Professor since January 2008. From 2015 to 2018, he was the Head of the Department of Electrical and Electronic Engineering, University of Nottingham. He has authored/coauthored more than 700 academic publications in leading international conferences and journals.

Prof. Wheeler is currently the Head of the Power Electronics, Machines and Control Research Group, Global Director of the University of Nottingham's Institute of Aerospace Technology and was the Li Dak Sum Chair Professor in Electrical and Aerospace Engineering from 2016 to 2020. He is a member of the IEEE PEL's AdCom and was an IEEE PELS Distinguished Lecturer from 2013 to 2017